

# GEANT4 SIMULATION FRAMEWORK FOR CUSTOMIZABLE RADIOGRAPHY IMAGING

Miguel Comett<sup>ID</sup>, Daniel Pereira Sandino<sup>ID</sup>, Juan Pablo Solís Ruiz<sup>ID</sup>, Alonso Arriola Félix<sup>ID</sup>, Alberto A. Velasco<sup>ID</sup>, Luisa Fernanda Chaparro Sierra<sup>\*</sup><sup>ID</sup>, J.A. García-González<sup>\*</sup><sup>ID</sup>

Tecnológico de Monterrey, School of Engineering and Sciences

## ABSTRACT

Nowadays there is an increasing need for simulated images that accurately mimic real-world scenarios to drive innovation and improve existing techniques in medical imaging. This demand is met by rapidly cost-effectively iterating on various configurations.

Geant4 enables realistic simulations of X-ray radiography and tomography by modeling the X-ray source and detector. At the same time, Python handles data processing and analysis, resulting in an efficient and adaptable workflow.

Endorsed by the scientific community for medical physics applications, Geant4 faithfully replicates the relevant interactions to medical imaging. Scaling to medium-sized servers allows for fast simulation production.

A customizable framework has been developed with capabilities that include X-ray spectrum characterization, attenuation coefficient calculations for any material, radiography, and tomography generation, allowing image processing using the DEXA method to decompose materials, as shown in this report as an example of the tool's usage.

**Index Terms**— Geant4, Attenuation Coefficient, CNR, DEXA, CT Scan, Medical Imaging.

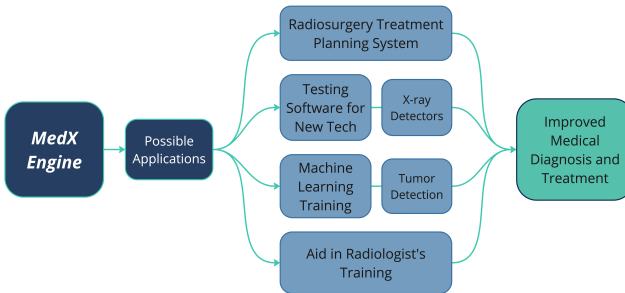


**Fig. 1.** Visual Objectives of the Investigation.

## 1. INTRODUCTION

Generating accurate and reliable images is crucial for driving advancements in medical imaging, particularly in the early

diagnosis of various diseases, where timely detection can significantly improve clinical outcomes. Techniques such as conventional X-ray radiography, DEXA (Dual-Energy X-ray Absorptiometry), and CT (computed tomography) scans offer detailed visualizations of internal body structures, enabling more precise and prompt diagnoses.

Software tools like Geant4, a robust toolkit developed by CERN (European Organization for Nuclear Research) that facilitates multi-level computational simulations; GATE (a Geant4-based application), Penelope, and others provide advanced simulation capabilities for particle interactions with matter, particularly in fields like medical physics and nuclear research. Geant4 and GATE are the most extensively cited in the literature [1], reflecting their widespread adoption and reliability. In this context, Geant4 emerges as an attractive toolkit for simulating X-ray imaging [2].

Various frameworks, such as radiography and tomography, have been developed for image generation and are primarily used in manufacturing studies and advanced materials evaluation. One example is the software Novi-sim, which utilizes the Gate engine for simulating radiography and CT scans. However, Novi-sim has limitations in its physics and is more focused on manufacturing and materials applications than medical use [3].

This work introduces a framework developed using Geant4 capable of generating a large volume of high-resolution images and 3D reconstruction of various anatomical regions. A simple CNR (contrast to noise ratio) enhancement using DEXA and a CT scan of a custom-made thorax are present in this report as examples of its utilization. This framework not only facilitates the generation of detailed and precise images, but it could also be ideal for advanced applications such as training machine learning models [4], as it can generate massive images of any loaded phantom, broadening its application to advanced diagnostic techniques.

### 1.1. State of the art

Planning and simulation systems in radiology have advanced significantly with the development of new technologies in image processing, artificial intelligence (AI), and clinical workflow optimization. These tools enable more accurate diagnoses and better-targeted treatments, which are crucial for

\* Corresponding authors. lchaparr@tec.mx

the effective management of various diseases [5]. An essential component is image segmentation to identify anatomical structures and pathologies, an area where deep neural networks like U-Net have significantly improved accuracy in identifying tissues and lesions [6]. This enhances intervention planning and the customization of treatments, especially in oncology [7]. Regarding radiation dosing, simulations based on the Monte Carlo method are essential for accurately calculating radiation distribution in tissues. Despite their high computational cost, this method, integrated into tools like Geant4, remains the standard in radiotherapy [8].

## 2. METHODOLOGY

The process was divided into two key stages. The first stage focuses on computational simulation architecture, while the latter centers on data processing.

### 2.1. Simulation in Geant4

#### 2.1.1. Geant4 Architecture

Figure 3 shows the workflow of a simple Geant4 program. The main classes are Geometry, Particle Generator and the Physics Lists (green squares). These classes are managed by the Run Manager. For it is a Monte Carlo simulation tracking what happens is the most important characteristic [9]; the Stepping Action tracks the path of every particle generated and their interactions are called events.

#### 2.1.2. Simulation Setup

This report's sample is a custom-made thorax designed to emulate soft tissue, a rib cage, lungs, and a heart made of muscle. Figure 4 shows the computational simulation setup, where the source-target-detector geometry is shown. The particles are photons, the skin-muscle-adipose layer, and lungs are made of G4-TISSUE-SOFT-ICRP whereas the rib cage is made of G4-B-100 BONE, both Geant4 materials. The particle detector's material is negligible since reporting the changes in detector characteristics is not the focus of this work.

#### 2.1.3. Simulated X-ray Vacuum Tube

The capability of using a real X-ray spectrum as a particle source is studied using Idrissi's G4XRTube Geant4 application [10]. A simulated x-ray spectrum was obtained using a 1.3mm aluminum filter and a tungstate anode for 80 and 140 kVp. However, this work uses the monochromatic mode with 40 and 80 keV for simplicity.

#### 2.1.4. Attenuation Coefficient

The analysis of attenuation coefficients is crucial to how photons interact with certain materials, which is a key factor in

obtaining images. Using an algorithm to change the thickness of a material based on an arbitrary percentage of transmitted photons, we can calculate the mass attenuation coefficient using Eq.1 as a function of energy, where  $\rho$  is the material density,  $d$  thickness,  $N$  total number of emitted photons and  $N_o$  the number of transmitted photons.

$$\mu_\rho = -\frac{1}{\rho d} \ln \left( \frac{N}{N_o} \right) \quad (1)$$

A calibration test was performed to validate the results because there is no standard attenuation coefficient for the used bone material and soft tissue. In Figure 5, the simulated coefficients (dots) are almost identical to the real data (solid lines) obtained from a medical database [11] for skin, muscle, and adipose materials for energies from 20keV to 100keV. Our algorithm predicts the behavior of those coefficients, so we infer that it will also predict the behavior of non-recorded materials like Geant4 bone (black dots) and soft tissue (purple dots).

#### 2.1.5. Radiation Dose

While performing an scan, it is fundamental to consider and utilize the least possible radiation dose that yields a good projection, in order to prevent unintended damage to healthy cells. The common, accepted dose for a chest radiography is 0.02 mGy, and 8 mGy for a chest CT [12].

In Geant4, the dose calculation is performed as the ratio between the energy deposition and the mass of the irradiated area. The energy deposition is the portion of the x-ray's energy that has not gone through and thus has been absorbed by the patient's tissue.

$$Dose = \frac{\text{Energy Deposition } [J]}{\text{Sample Mass } [kg]} \quad (2)$$

The radiation dose for the DEXA projection, as described in section 2.2.1 is calculated with the parameters in the table below. The thorax model has a mass of 23.98 kg. The total dose is the addition of the individual doses for the two energy radiography.

Number of Photons	Energy of Photons	Energy Deposition	Radiation Dose
$2.4 * 10^{10}$	40 keV	318.19 TeV	0.0021 mSv
$2.4 * 10^{10}$	80 keV	636.39 TeV	0.0042 mSv
Total Dose:			0.0063 mSv

This calculation being made for a monochromatic X-ray source and a perfect detector, is not representative of reality. It is straight forward to factor a detector's efficiency of 80%,

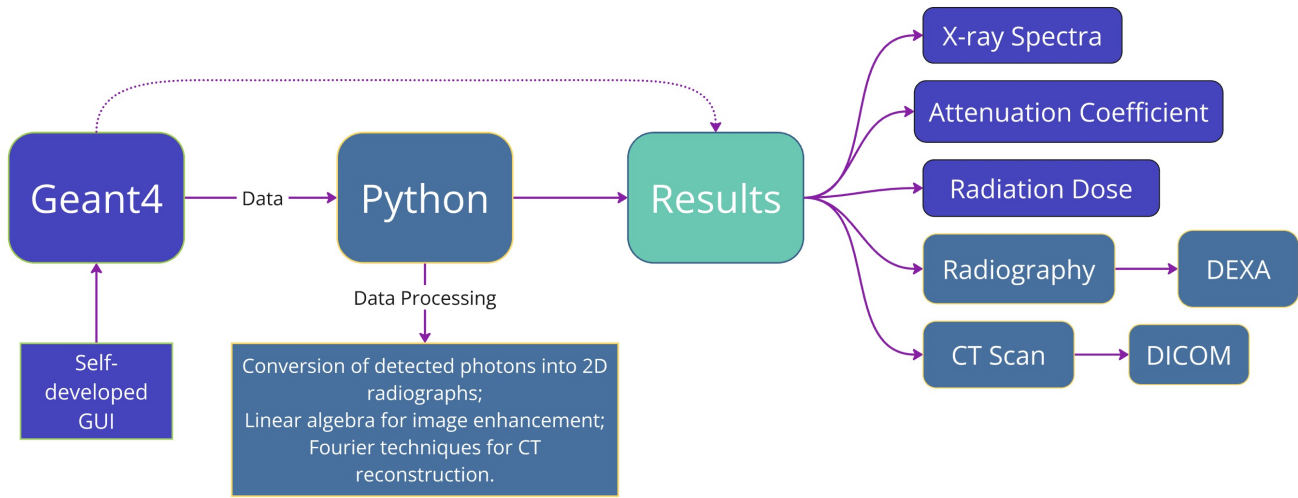


**Fig. 2.** Functionality of the GUI. Data is generated through simulation in Geant4 and processed using a Python script, which allows for obtaining a wide variety of results for different analyses.

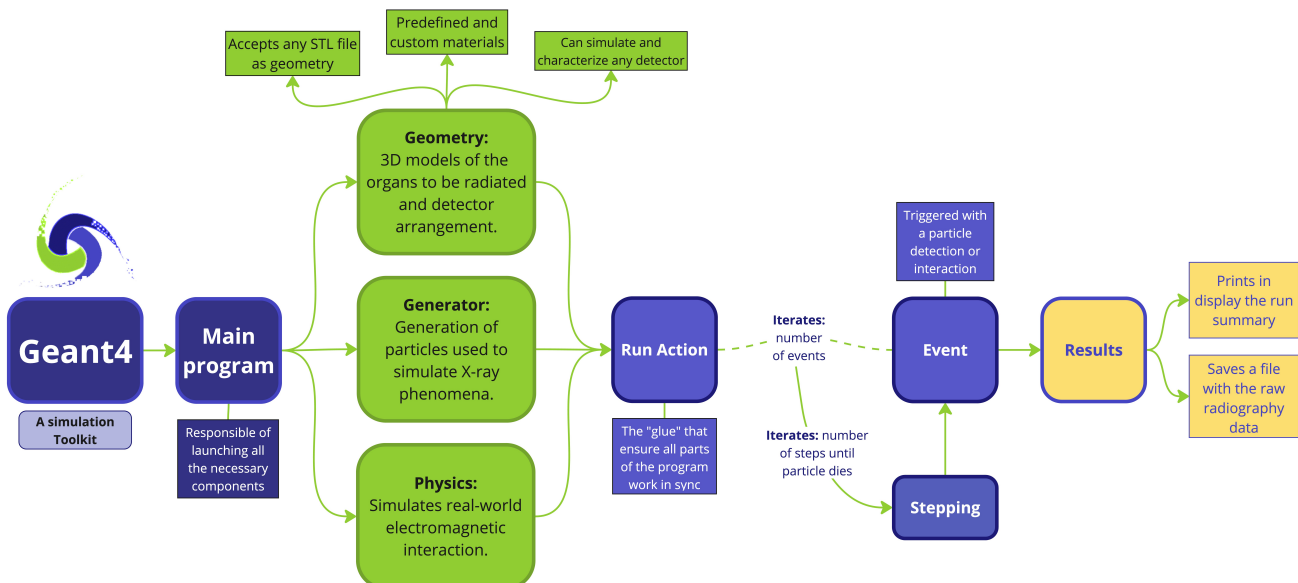


**Fig. 3.** Geant4 consists of core components like the geometry module, the physics module, and the event generation and tracking module. All regulated by the run action.

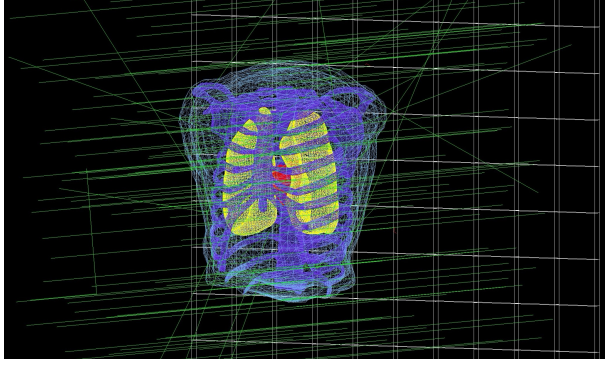


**Fig. 4.** Geant4 geometry setup. The photon's trajectories are represented as green lines. The thorax has a white cloud for soft tissue, green for the lungs, blue for bone ribcage, and red for the heart. The detector is a rectangular prism behind the thorax.

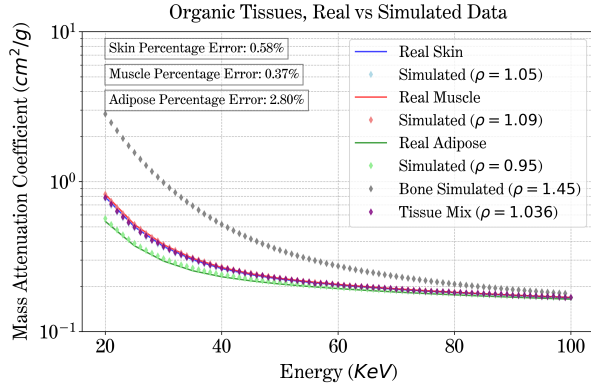


**Fig. 5.** Attenuation coefficients for recorded data (solid lines) and experimentally obtained (dots) of skin (blue), adipose (green), and muscle (red) materials. The global errors are 0.58%, 0.37%, and 2.80% respectively.

as well as an 80 and a 140 kVp X-ray source, to achieve a more realistic dose estimation.

This considerations result in a dose of 0.0106 mSv, which is still lower than expected (0.02 mSv), and could be attributed to the fact that our simulation takes ideal environmental conditions.

#### 2.1.6. Pathologies

An additional feature being developed for the Geant4 framework is the ability to simulate tissue pathology. The team is working in simulating neoplastic tissue by inputting the desired geometry and tissue properties for specific tumors. Moreover, a feature that lets the user modify parameters of tissue density in bones is also being developed. This will add to the framework the capability to simulate osteoporosis and related bone conditions.

## 2.2. Data Processing in Python

It is important to have a quantitative measure of contrast since it shows the capability and effectiveness of the radiologist in identifying pathologies. The Contrast to Noise Ratio (CNR) in a medical image is a measure of the difference between the Region Of Interest (ROI) and the background [13].

$$CNR = \frac{S - B}{\sigma_B} \quad (3)$$

$S$  stands for the ROI signal and  $B$  for the background value.

### 2.2.1. Dual Energy X-ray Absorptiometry (DEXA)

Recalling Figure 5, the difference between the attenuation coefficient of bone and organic tissues at low energies is much bigger than at higher ones. Exploiting this fact, two images are obtained at low and high energies for dual-energy (DE) image decomposition.

DE image decomposition algorithms have been well studied and documented [14]. A simple one is called Standard Log Subtraction (SLS), described as follows:

$$I_{SLS}(x, y) = -wI_L(x, y) + I_H(x, y) \quad (4)$$

where  $w = \mu_H/\mu_L$ , is called the tissue cancellation parameter, equal to the ratio between the linear coefficients of the canceled material at high and low energy.  $I_H$ ,  $I_L$  are the natural logarithmic projections at high and low energy, respectively, as described in Eq.7.

Taking the SLS method further, the Anti-Correlated Noise Reduction (ACNR) method takes advantage of the fact that quantum noise in the soft-tissue and bone-only image is anti-correlated. [15].

$$I_{ACNR} = I_{SLS}(x, y) + [I_{SLS}^c(x, y) * h_{HPF}(x, y)] \quad (5)$$

where  $h_{HPF}$  denotes the high-pass filter. In the Fourier domain, the used Gaussian filter is defined as:

$$H_{HPF}(u, v) = 1 - \exp\left(-\frac{u^2 + v^2}{2d_{HPF}^2}\right) \quad (6)$$

### 2.2.2. CT Scan

The setup for the CT scan is configured to simulate parallel beam projection, acquiring radiographic images while rotating the target with a user-defined angle step. The obtained images are then corrected for the exponential attenuation characteristics by undergoing logarithmic transformation. This leads to the projection measurements for every detector element,  $I$ , corresponding to linear sums of the coefficients through the simulated thorax along the rays' path [16].

$$I = \ln \left[ \frac{J_0}{J} \right] = t (\mu_1 + \mu_2 + \mu_3 + \dots + \mu_n) \quad (7)$$

where  $J_0$  is the intensity reading outside the field of view of the thorax,  $J$  is the reading at the detector element, and  $t$  and  $\mu$  are the thickness and linear attenuation coefficient that the rays travel through before being detected.

These projection measurements are then converted into slices, solving for the coefficients through inverse Radon reconstruction using the *schikit-image* library in Python. These obtained reconstructed slices are then converted into DICOM format using the *pydicom* library and exported to the medical imaging software 3DIMViewer.

### 3. RESULTS

#### 3.1. Simulated X-ray Spectra

In Figure 6, the simulated X-ray spectra is shown using G4XRTube. For its usage the user must obtain the spectra via X-ray spectra online generators [17] or other sources and then it can be used in this framework.

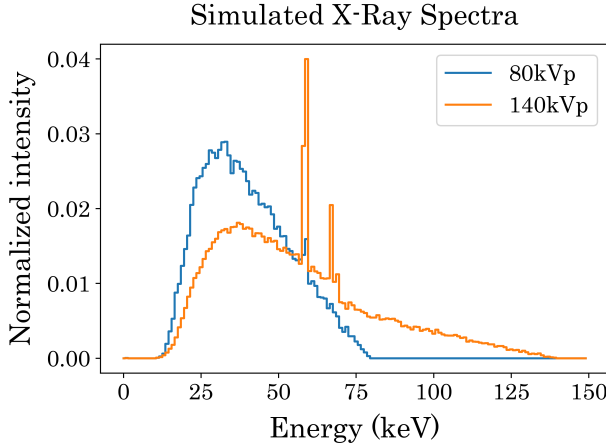


**Fig. 6.** The simulated x-ray spectrum used for 80 (blue) and 140 (orange) kVp with a 1.3mm aluminum filter thick and a tungstate anode.

#### 3.2. Dual Energy X-ray Absorptiometry (DEXA)

Figure 7 shows the obtained images from a DE simulation using 40 and 80 keV with  $1 \times 10^8$  photons. The low-energy image (left) displays the full thorax, including the rib cage, lungs, and heart. Two regions of interest (ROIs) are analyzed: the blue rectangle represents the signal area (bone), while the red rectangle marks the background (heart). The contrast between these areas was analyzed using Eq.3 to calculate the CNR value. In Figure 5, at 40 keV, bone attenuation is significantly higher than that of muscle and soft tissue; consequently, high contrast between these materials was expected. The obtained CNR value of 5.84 aligns with this expectation, confirming the anticipated contrast level.

After applying the ACNR filter using Eq.5 in both low and high energy images with a  $w = 0.677$ , the bone and tissues were decomposed. The bone-decomposed image (center) shows less contrast between the same ROIs as in the low-energy image, with a CNR of 2.80; however, the heart is less visible. In contrast, the tissue-decomposed image demonstrates effective separation from bone, clearly distinguishing soft tissues from bone structures.

#### 3.3. CT Scan

CT reconstructed axial and coronal slices for the thorax model are shown in Figure 8. Each material's different linear attenuation coefficients, expressed in Hounsfield units, match the values calculated during the previous simulations introduced in section 2.1.4.

The pixel spacing for the reconstructed axial slices is 0.5 mm, corresponding to the simulated radiographic images. To obtain a slice thickness of 0.5 mm, 300 slices were reconstructed. The volumetric visualization is shown in Figure 9, where the upper thoracic structure of the model is accurately reconstructed.

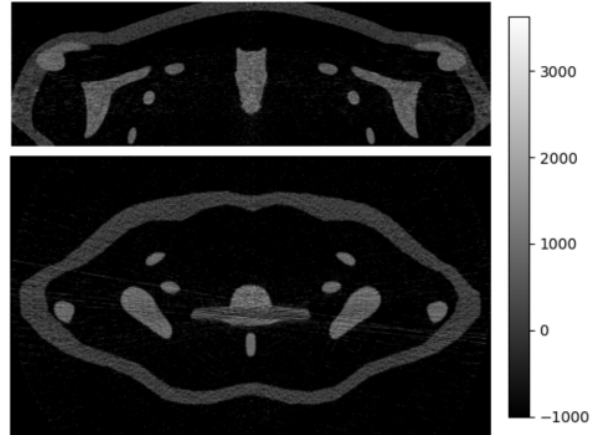


**Fig. 8.** Coronal (top) and axial (bottom) computed tomography slices of the simulated thorax and ribcage. Grayscale values are expressed in Hounsfield units (HU).



**Fig. 9.** Volumetric 3D reconstruction of the upper thoracic skeletal structure.

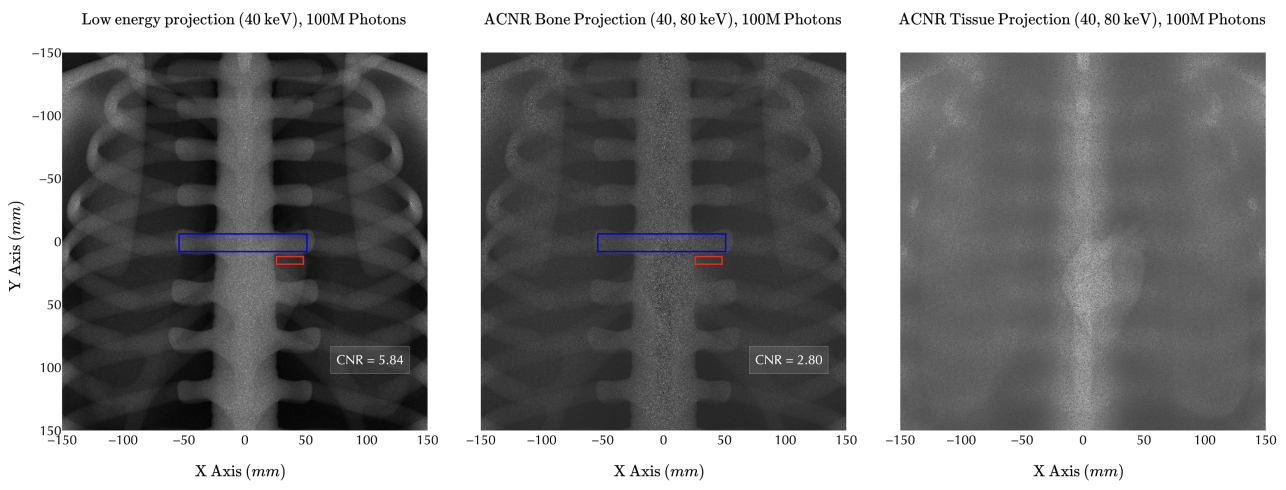


**Fig. 7.** The ACNR technique is compared to the single energy image simulated. We observe in the middle figure that the heart and lungs have almost completely been eliminated. The third image highlights the heart and lungs, and the bones fade.

#### 4. CONCLUSIONS

Enhancing CNR through DEXA images applying a simple ACNR filter was not achieved. The reduction in CNR is likely due to the simplicity of the 3D model and the lack of advanced algorithms needed for substantial contrast-to-noise improvement. However, the method was successful in achieving effective tissue decomposition, enabling clear differentiation between bone and soft tissues. Additionally, the 3D reconstruction of the thorax with CT imaging was successfully implemented. Analysis in images obtained for certain pathologies still has to be performed and studied.

#### 5. ACKNOWLEDGMENTS

The authors thank Tecnológico de Monterrey for providing access to the computational resources to develop this work.

**Financial Disclosure:** The authors have no relevant financial or non-financial interests to disclose.

**Compliance with Ethical Standards:** This is a simulation study for which no ethical approval was required.

#### 6. REFERENCES

- [1] Michelle Chen, Maria Gerges, William Y. Raynor, Peter Sang Uk Park, Edward Nguyen, David H. Chan, and Ali Gholamrezanezhad, “State of the art imaging of osteoporosis,” *Seminars in Nuclear Medicine*, vol. 54, no. 3, pp. 415–426, 2024, Musculoskeletal Disorders.
- [2] Molly Kirkpatrick, Sean Hood, Susanna Guatelli, and Yves Van Haarlem, “Comparing the output of measured and geant4 simulated x-ray tubes,” *Radiation Physics and Chemistry*, vol. 220, pp. 111647, 2024.
- [3] Neffati D. et al., “Novi-sim: A fast x-ray tomography simulation software for lab and synchrotron systems,” in *12th Conf. on Industrial Computed Tomography (iCT)*, 2023, 2023, vol. 28.
- [4] Ana Barragán-Montero et al., “Artificial intelligence and machine learning for medical imaging: A technology review,” *Physica Medica*, vol. 83, pp. 242–256, 2021.
- [5] Hongyu Kang, Wei Zhang, Shuai Li, Xinyi Wang, Yu Sun, Xin Sun, Fang-Xian Li, Chao Hou, Sai Kit Lam, and Yongping Zheng, “A comprehensive benchmarking of a u-net based model for midbrain auto-segmentation on transcranial sonography,” *Computer Methods and Programs in Biomedicine*, vol. 258, pp. 108494, 2025.
- [6] S. Guatelli, M.G. Pia, and M. Piergentili, “Technology transfer from hep computing to the medical field: overview and application to dosimetry,” *Nuclear Physics B - Proceedings Supplements*, vol. 150, pp. 13–18, 2006, Proceedings of the 9th Topical Seminar on Innovative Particle and Radiation Detectors.
- [7] T. Martín-Noguerol, F. Paulano-Godino, R. López-Ortega, J.M. Górriz, R.F. Riascos, and A. Luna, “Artificial intelligence in radiology: relevance of collaborative work between radiologists and engineers for building a multidisciplinary team,” *Clinical Radiology*, vol. 76, no. 5, pp. 317–324, 2021.
- [8] Harsha Latha P, S. Ravi, and Saranya A, “Breast cancer detection using machine learning in medical imaging –

- a survey,” *Procedia Computer Science*, vol. 239, pp. 2235–2242, 2024, CENTERIS – International Conference on ENTERprise Information Systems / ProjMAN - International Conference on Project MANagement / HCist - International Conference on Health and Social Care Information Systems and Technologies 2023.
- [9] Robert L. Harrison, “Introduction to monte carlo simulation,” *National Institute of Health*, 2010.
  - [10] Abdelghani Idrissi, Ibrahym Dourki, T. El Bardouni, O. El Hajjaji, Mohamed Drissi El-Bouzaidi, and Mohamed Mira, “G4xrtube: A geant4-based monte carlo application for x-ray tube simulation,” *Radiation Physics and Chemistry*, vol. 207, pp. 110864, 2023.
  - [11] “X-ray complex refraction coefficient,” <http://ts-imaging.science.unimelb.edu.au/Services/Simple/ICUtilXdata.aspx>, 2024.
  - [12] Madan M Rehani and Manorma Berry, “Radiation doses in computed tomography,” *BMJ*, vol. 320, no. 7235, pp. 593–594, 2000.
  - [13] Catherine Westbrook, *MRI at a glance*, John Wiley Sons, 3 edition, 2016.
  - [14] Daniel J. Tward Samuel Richard, Jeffrey H. Siewerdsen, “Neq and task in dual-energy imaging: From cascaded systems analysis to human observer performance,” *Proceedings of SPIE - The International Society for Optical Engineering*, 2008.
  - [15] Thomas, “Improvement of material decomposition and image quality in dual-energy radiography by reducing image noise,” *Proceedings of SPIE - The International Society for Optical Engineering*, 2016.
  - [16] Jerrold T. Bushberg, J. Anthony Seibert, and Edwin Leidholdt Jr., *The Essential Physics of Medical Imaging*, Lippincott Williams & Wilkins (LWW), 4th edition, 2020.
  - [17] Department of Medical Physics, University of Crete, Faculty of Medicine, “X-ray spectrum generator for monte carlo calculations,” Online; Contact: Prof. John Damilakis, n.d.